

Two-Color Single Hybrid Plasmonic Nanoemitters with Real Time Switchable Dominant Emission Wavelength

Xuan Zhou,[†] Jérémie Wenger,[†] Francesco N. Viscomi,^{†,‡} Loïc Le Cunff,[†] Jérémie Béal,[†] Serguei Kochtcheev,[†] Xuyong Yang,[§] Gary P. Wiederrecht,^{||} Gérard Colas des Francs,[⊥] Anu Singh Bisht,[†] Safi Jradi,[†] Roberto Caputo,[‡] Hilmi Volkan Demir,[§] Richard D. Schaller,^{||} Jérôme Plain,[†] Alexandre Vial,[†] Xiao Wei Sun,^{*,§} and Renaud Bachelot^{*,†}

[†]Laboratoire de Nanotechnologie et d'Instrumentation Optique, ICD, CNRS UMR 6281, Université de Technologie de Troyes, 12 Rue Marie Curie CS42060, 10004 Troyes Cedex, France

[‡]Department of Physics & CNR-NANOTEC University of Calabria, I-87036 Rende, Cosenza, Italy

[§]School of Electrical and Electronic Engineering, Nanyang Technological University, Nanyang Avenue, Singapore 639798

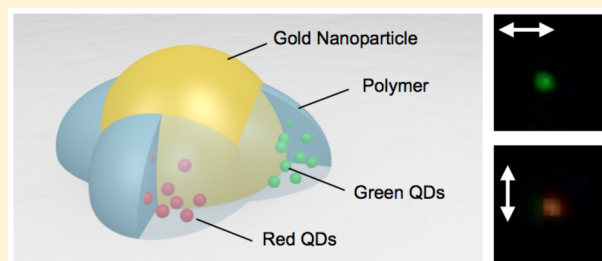
^{||}Center for Nanoscale Materials, Argonne National Laboratory, 9700 S. Cass Avenue, Lemont, Illinois 60439, United States

[⊥]Laboratoire Interdisciplinaire Carnot de Bourgogne (ICB); UMR 6303 CNRS, Université de Bourgogne, Franche-Comté, 9 avenue Alain Savary BP 47870, F-2178 Dijon Cedex, France

S Supporting Information

ABSTRACT: We demonstrate two-color nanoemitters that enable the selection of the dominant emitting wavelength by varying the polarization of excitation light. The nanoemitters were fabricated via surface plasmon-triggered two-photon polymerization. By using two polymerizable solutions with different quantum dots, emitters of different colors can be positioned selectively in different orientations in the close vicinity of the metal nanoparticles. The dominant emission wavelength of the metal/polymer anisotropic hybrid nanoemitter thus can be selected by altering the incident polarization.

KEYWORDS: nanoemitter, hybrid nanostructures, fluorescence spectroscopy, nanophotonics, surface plasmons, photopolymerization



Modern information and communication technologies require higher bandwidth and greater energy efficiency in order to face the challenge of the increasing amount of data traffic. In this context, optical data is the key: the fast development of integrated optics and nanophotonics has steadily produced more optical functionality in a small chip.^{1,2} This continued development of nanophotonics requires integration of efficient optical nanosources (including multi-color sources for future nanoscale multiplexing) that are able to address and activate specific parts of the circuit. In this regard, hybrid plasmonic nanosources, including plasmon lasers, are a recent promising solution.^{3–6}

This Letter introduces a new type of hybrid plasmonic nanoemitter. Research on plasmonic nanoemitters has garnered great interest. The essential concept for these systems is the energy transfer, including radiative and nonradiative processes, between the metal nanostructure and adjacent components that include semiconductor quantum dots^{7,8} or dye molecules.^{9–11} Numerous fundamental research advances have been carried out to understand the relevant photophysical processes in these hybrid nanomaterials, such as the Purcell effect.^{6,12} Reported studies show that for a given quantum emitter, the output spectra of the plasmonic nanoemitters depend on many

parameters: the size and shape of the metal nanoparticles^{11–16} or nanoapertures,^{17,18} the surface plasmon modes,¹⁹ the dipolar orientation²⁰ of quantum emitters, as well as the separation between the nanoparticle and dipole emitters.^{21–23} As a result of these fundamental studies, different high performance light-emitting plasmonic hybrid nanosystems have begun to emerge based on, for example, metal core/doped shell,^{24,25} metal bowties,¹⁶ antennas,⁶ Yagi-Uda optical antennas,²⁶ and dimer antenna.²⁷ Other emerging methods based on one-photon near-field polymerization²⁸ and biomolecular functionalization^{9,21,29,30} have been used to fabricate plasmonic nanoemitters.

Despite these numerous achievements, most of the reported hybrid nanoemitters contain only a single output color. In classical nanoplasmonics (with no coupling with an emitter), a single color can be easily tuned either by modifying parameters such as size, shape and environment³¹ or by using specific effects such as near-field coupling³² and mode hybridization.³³ On the other hand, two-color approaches rely on the spatial

Received: July 31, 2015

Revised: September 25, 2015

Published: October 5, 2015



anisotropy of single or coupled metal nanostructures, resulting in a symmetry breaking splitting of the dipolar plasmon modes that can be selected by the incident polarization.^{34–37} However, in these cases, no quantum emitters are involved, making the control of emission quantum yield and lifetime impossible. In hybrid plasmonics involving emitters, changing the color of emission requires changing the dyes. Two different fluorophores were mixed by L. Zhao et al., resulting in a controlled energy transfer between the donors and the acceptors in the vicinity of metal nanocrystals.³⁸ X. Meng et al. reported a hybrid spaser whose wavelength can be tuned in the 562–627 nm range by changing the dye concentration.³⁹ Nevertheless, in ref 38, the nanoscale spatial distribution between the two fluorophores was not controlled and the emission wavelength of the hybrid structure was not selectable. In ref 39, for a given dye concentration, the peak wavelength was fixed and not tunable. Additionally, in ref 39 and in most of the other references on the subject, single hybrid nanoparticles were not addressed and the collected signal came from an ensemble of nanoparticles, which can induce some unwanted effect due to interaction between nanoparticles. As a conclusion of the short state of the art, no two-color single hybrid plasmonic nanosource having real-time color tunability has been reported so far.

Our research aims at developing hybrid multicolor nanoemitters whose specific emission mode (i.e., output color) can be externally selected and controlled in real time. In this Letter, we report on single anisotropic hybrid nanoemitters that position two different quantum emitters in different locations surrounding a metal nanoparticle in such a manner that the emission colors can be selected by changing the polarization of incident excitation light. Fabrication of the two-color anisotropic nanoemitters (TCANEs) is based on the plasmonic two-photon polymerization (TPP) of a formulation that contains quantum dots (QDs).

QD-Grafted Two-Photon Polymerizable Solution. The polymerizable solutions were made up of 1 wt % Irgacure 819 (IRG 819) and 99 wt % QDs-grafted pentaerythritol triacrylate (PETIA). Two different types of QDs were used: CdSe/ZnS (Figure 1a) and CdSe/CdS/ZnS (Figure 1b) that emit in the green and in the red, respectively. Figure 1a,b show micron-size polymer patterns made by far-field scanning TPP of the hybrid formulation (using the commercial laser writing system from Nanoscribe GmbH). Figure 1c is a scanning electron microscope (SEM) image of the selected region (white rectangular) selection of the micron-size pattern in Figure 1a. The fluorescence spectra shown in Figure 1d were collected from green QD-grafted PETIA (black) and red QD-grafted PETIA (red) solutions. During TPP, IRG 819 was used as a photosensitizer. A femtosecond laser ($\lambda_0 = 730$ nm) was selected as the curing light source for TPP in order to match the absorption of the IRG819 that shows a peak at 365 nm.⁴⁰

In a typical photopolymerization process, light induces the polymerization reaction when the exposure energy dose exceeds a given threshold D_{th} . For plasmonic near-field TPP, an exposure dose below the polymerization threshold D_{th} was instead used. This is to guarantee the selective integration of polymer structures in the close vicinity of the nanostructures by surface plasmons, which enhance the local dose of the electromagnetic field that locally exceeds the polymerization threshold.^{41–46} In our experiments, we used an incident dose of $D_0 = 60\%D_{th}$. Because QDs were grafted onto the monomer in solution, they can therefore be firmly trapped in the

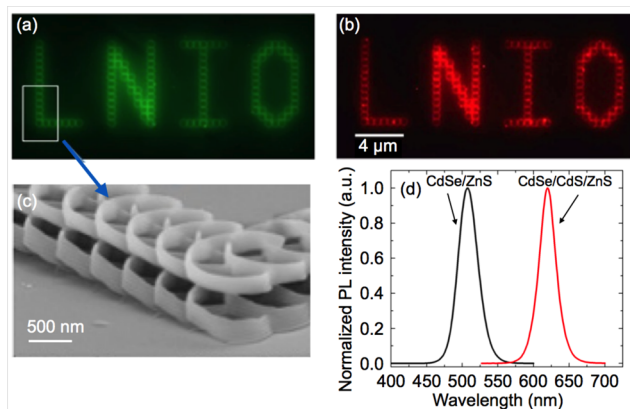


Figure 1. QD containing photopolymerizable formulation on an ITO-coated glass substrate without the presence of metal nanoparticles. (a) Fluorescence image of a photopolymerized micron-size pattern doped with CdSe/ZnS (green QDs). (b) Fluorescence image of a photopolymerized micron-size pattern doped with CdSe/CdS/ZnS (red QDs). (c) SEM image of the rectangular selected region of the micron-size polymer pattern. (d) Photoluminescence (PL) spectra from green QD-grafted PETIA (black) and red QD-grafted PETIA (red) solutions. For fluorescence excitation, the wavelength was set at $\lambda_{exc} = 405$ nm.

photopolymer. The remaining unpolymerized QD-grafted solution was removed by rinsing with acetone for 10 min and isopropanol for 5 min. Gold nanodisks and gold nanostars were used to fabricate the TCANEs.

Gold Nanodisk-Based TCANE. Nanodisks were considered in this experiment for their highly symmetric geometry in the XY plane (Figure 2a). The gold nanodisks were fabricated by electron-beam lithography (EBL) on a glass substrate that was coated with a 3 nm thick layer of ITO. The space between two adjacent nanodisks is 2.5 μm , which is large enough for the upcoming spectra collection from single nanoparticle. Figure 2a shows a SEM image of an initial single gold nanodisk (90 nm in

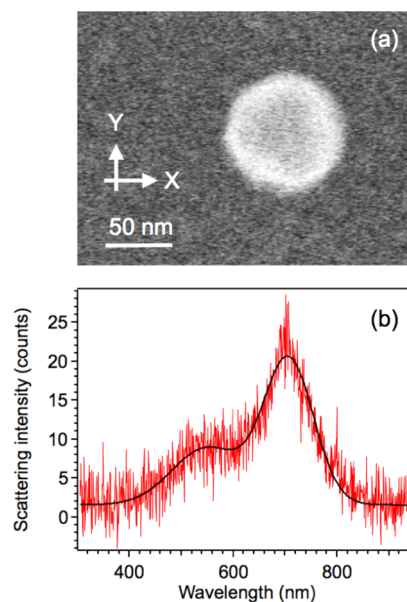


Figure 2. Characterization of a gold nanodisk. (a) SEM image of a gold nanodisk of $d = 90$ nm in diameter. (b) Scattering spectrum in air showing the surface plasmon resonance of the nanodisk before TPP.

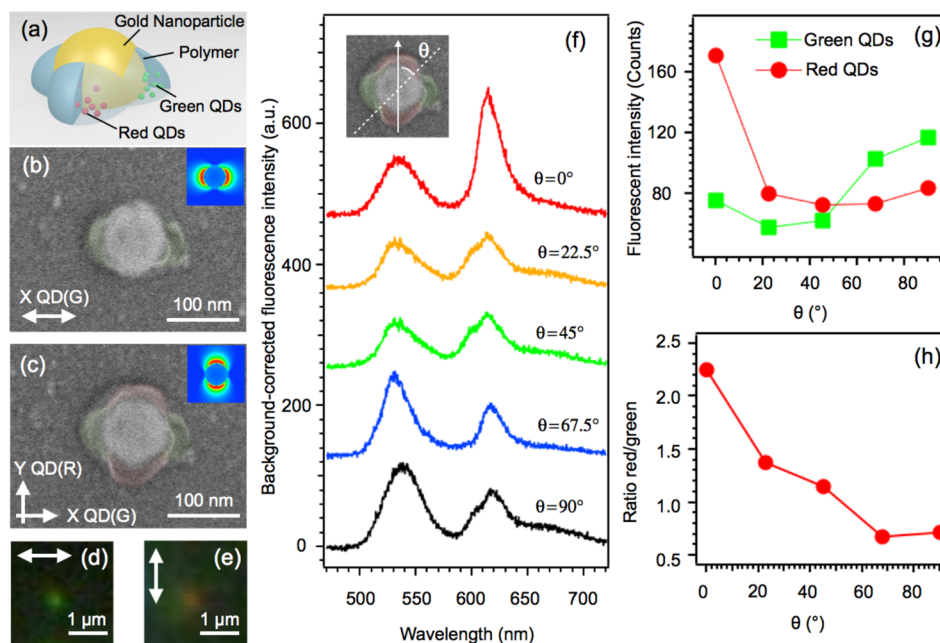


Figure 3. Nanodisk-based two color anisotropic nanoemitter: topographic and optical characterizations. (a) Schematic representation of the nanostructure. (b) SEM image of the Au nanodisk of $d = 90$ nm after the first exposure that positions green QDs along the X axis (plasmonic near-field intensity of dipole emission for polymerization is shown in the inset). (c) SEM image of the same nanodisk after the second exposure that traps red QDs along the Y axis (plasmonic near-field intensity of dipole emission for second exposure is shown in the inset). For clarity, SEM images have been artificially colored according to the emission wavelengths of the trapped QDs. The original SEM images are provided in the [Supporting Information](#). Far-field fluorescence image of the TCANE under illumination with (d) X axis polarization and (e) Y axis polarization. Double arrows represent the polarization of the excitation light. (f) Polarization-dependent fluorescence spectra from the TCANE. The polarizations of the excitation light ($\lambda_{\text{exc}} = 405$ nm) were at $\theta = 0^\circ$ (red plot), 22.5° (orange), 45° (green plot), 67.5° (blue plot), and 90° (black plot) with respect to the Y axis. The inset defines the polarization angle θ . The dashed line represents the incident polarization direction. (g) Intensities of emission peaks of the green QDs (green square) and red QDs (red dot) as a function of polarization angle. (h) Ratio of intensity of red/green as a function of polarization. The excitation wavelength was set at $\lambda_{\text{exc}} = 405$ nm for fluorescence images and spectra.

diameter and $h = 50$ nm in height) before performing any two-photon polymerization procedure. [Figure 2b](#) is the scattering spectrum of the nanodisk in air. The main peak at 700 nm represents the dipolar mode of surface plasmons, whereas the shoulder around 540 nm corresponds to the quadrupolar plasmon mode. The incident wavelength of $\lambda_0 = 730$ nm used for TPP thus matches well the plasmon resonance of the gold nanodisk when considering a slight redshift from the coating medium of photopolymerizable solution with $n = 1.48$ refractive index. More details on the reason for choosing 90 nm nanodisks are provided in the [Supporting Information](#).

[Figure 3a](#) shows a scheme of the TCANE. The fabrication procedure consisted of two steps. The first step was to polymerize along the X axis to position green QDs in the X direction. The incident dose, as mentioned above, was set at $D_0 = 60\%D_{\text{th}}$. The obtained hybrid nanostructure was characterized using SEM. Metal and polymer show different contrasts on the SEM image ([Figure 3b](#)). The polymer nanostructures can be recognized easily along the X axis in the vicinity of the nanodisk, as a polymer replica of the dipolar near-field intensity. After obtaining an anisotropic hybrid nanoemitter with green QDs positioned along the X axis, we performed the second exposure by coating the same sample with the red QD-grafted solution and exposing the same particle to a curing light ($\lambda_0 = 730$ nm) with an incident polarization oriented along the Y axis. The normalized dose D_0/D_{th} in the second exposure was again 60%. It was maintained at the same level as the normalized dose in the first exposure so that the integrated red QD-containing photopolymer region was approximately the same size of the

green QD-containing photopolymers. As a result, [Figure 3c](#) show the SEM images of the nanodisk ($d = 90$ nm) after the second polymerization along the Y axis. The distribution of the green QD-grafted photopolymers can be clearly distinguished from the red QD-grafted photopolymers by comparing these two SEM images. On the basis of the SEM images recorded at both steps, it turns out that the two different QD-grafted photopolymers were selectively integrated in different orientations around the gold nanodisk via near-field plasmonic TPP. The presence of the QDs has been illustrated by the false colors added to the SEM images. The signature of this selective spatial positioning of the QDs is shown by the far-field fluorescence images of single TCANE ([Figure 3d,e](#)). For a first demonstration, the excitation wavelength was set at 405 nm and was therefore an off-plasmon resonance excitation. The optimized wavelength to use for effective plasmonic response is 730 nm, whereas the maximum absorption of QDs is in deep UV (refer to [Supporting Information](#)). To be more precise, QDs will not be excited at 730 nm, where the gold nanoparticles can be excited on their plasmon resonances. On the contrary, the QDs will be excited mainly by the incident far-field if UV light source is applied. However, in this case Au nanoparticles will go through interband transition and the plasmonic effect will be very weak. 405 nm is a compromise between the two aspects. Two-photon excitation is also possible for future fluorescence studies. Here, in this Letter, with one photon fluorescence excitation, the compromise between efficient plasmonic response and high absorption from QDs will have to be assessed. Despite the fact that this 405 nm

wavelength is still in the gold interband transition, it allows for polarization-dependent field confinement, as will be seen in the theoretical section. With an incident polarization along the X axis, the TCANE emits mainly in green (Figure 3d). In contrast, when the polarization of incident light is oriented along the Y axis, the emission in red dominates (Figure 3e). The output color selection of the TCANE using incident polarization is thus clear. The images illustrate an important result: for the first time, the color from a hybrid plasmonic emitter was tuned with polarization. By reading the RGB (red–green–blue) color code of both fluorescence images, a more direct analysis of the output color components can be carried out. The green-color dominant fluorescence signal can be decoded as (36, 112, 31), whereas the red is (95, 76, 28). In the conclusion, we will evoke some solution to increase the contrast between the three digits of this RGB code. The blue component comes from background (incident light) and is quite similar under different incident polarizations. The red component is more sensitive to the green as polarization flips. Figure 3e actually contains a non-negligible green component. This component makes the fluorescence image appear more likely to be orange than red. It has to be stressed that the blinking of QDs were observed (Supporting Information video of the fluorescence from green QDs doped in six TCANEs). However, instead of recording a completely dark period of TCANEs (i.e., sudden jump between maximum fluorescence intensity and 0), we obtained only a decrease of emission intensity (jump between maximum fluorescent intensity and a lower signal that is not 0). This indicates that in the lobes of each TCANE, not many QDs (but more than one QD) were trapped. Calculations, based on known concentration of QDs and an assessment of the volume of one QD, predict that about four QDs were trapped inside each polymer lobe. Blinking is a common effect of QDs that has not yet been reported to show any polarization dependence. In addition, the spectra acquisition time (20 s) is much longer than the time scale of QD blinking. Therefore, the blinking effect is not supposed to influence the relative intensity of green and red emission signals in our study.

More details regarding the control of the output can be obtained from the fluorescence spectra collected under different incident polarizations (Figure 3f). The fluorescence spectra show two emission peaks: 535 nm from green QDs and 620 nm from red QDs. The spectra may not reach an intensity as high as expected due to mainly two reasons. The first one is the fact that the signals were collected from a single nanoemitter and only a few QDs contributed in the spectra. The second reason is the ITO layer on the glass substrate reduces drastically the fluorescence signal. The reader is invited to refer to Supporting Information for a comparison between fluorescence signal from QDs on an ITO-coated substrate and QDs on a bare glass substrate. It is worth noting that the fluorescence peak of the green QD presents a slight red shift when the QDs are placed close to the nanodisk, as compared to the free space situation (Figure 1d). This redshift results mainly from a quadrupolar plasmon mode that has an enhancement effect, peaked at 540 nm, on the emission of green QDs. In other words, the spectral overlap between plasmon resonance of the nanodisk (540 nm) and free-space emission of QDs (510 nm) leads to a red shift of the emission peak of about 30 nm.

The polarization angle θ in the inset of Figure 3f defines the linear polarization of the excitation light with respect to the Y axis. Fluorescence signals were collected from the single

TCANE when $\theta = 0^\circ$ (red), 22.5° (orange), 45° (green), 67.5° (blue), and 90° (black). As the spectra illustrate, the fluorescence intensities of both QDs can be controlled by the incident polarization. At $\theta = 0^\circ$, the red QDs display the largest emission intensity as compared to other angles, and the ratio of red/green emission is at a maximum. At $\theta = 45^\circ$, the fluorescence signals of green and red emission modes show similar intensities. As the polarization angle increases to $\theta = 90^\circ$, the green emission mode starts to be dominant. This result is in good agreement with the fluorescence images in Figure 3d,e. To summarize, we show in Figure 3g fluorescence peak intensities of red and green QDs measured in Figure 3f as a function of polarization angle. The green QD emission shows lower intensity than red when $\theta < 45^\circ$, whereas a higher green emission than red was obtained when $\theta > 45^\circ$. In general, the emission of red QDs shows a decreasing trend, whereas green QDs show an increasing trend as a function of increasing θ . By plotting the ratio of red/green signals in Figure 3h, we see a decreasing trend of relative intensity between the two types of QDs as polarization angle increases. However, close inspection of Figure 3g reveals an unexpected small increase of the red emission between 67.5° and 90° and similarly an unexpected small decrease of the green emission between 0° and 22.5° . That is an anomalous (but small) increase of the emitted light at the perpendicular polarization. It should be pointed out that Figure 3g and e constitute first results that illustrate only a trend. For the moment, getting and controlling analytical expressions of light emission as a function of θ is not possible because this function would depend on three parameters: the exact number of QDs, their spatial position and their orientation within polymer nanolobes. At the time being, these three parameters are neither known nor controlled. The different zones in Figure 3g and e (including the anomalous increases and decreases in Figure 3g) are likely to be a signature of these three parameters. Further studies will allow us to address this issue.

The controllability of the dominant emission mode of TCANE originates from the optical selection of the anisotropically distributed QDs by rotating the position of the plasmonic near-field. This polarization dependence is a result of the spatial overlap of the dipolar plasmonic near-field, though excited out of the plasmon resonance, with the QD-grafted nanopolymers. When the incident polarization is oriented along the X axis ($\theta = 90^\circ$), the integrated photopolymer nanostructures doped with green QDs are completely overlapped with the near-field, while the structures doped with red QDs have a minimum spatial overlap with the plasmonic near-field. In contrast, when the incident polarization is oriented along the Y axis ($\theta = 0^\circ$), a minimum volume of the green QD-grafted photopolymer and a maximum volume of the red QD-grafted photopolymer are excited by the plasmonic near-field, resulting in a reduced emission in green but increased emission in red. This point of view will be illustrated further by the theoretical interpretation. It has to be stressed that, compared to red QDs, the emission of green QDs is less sensitive to the incident polarization as incident polarization varying from $\theta = 0^\circ$ to $\theta = 90^\circ$. More precisely, the fluorescent signal decrease of red QDs is 2.67 times greater than the signal increase of green QDs. Two reasons can be responsible for this phenomenon: (1) effective quantum yield of red QDs is higher than green QDs according to our simulation and (2) energy transfer from green QDs to red QDs at the interfaces of the adjacent polymer nanostructures (i.e., Förster resonant energy transfer, FRET).

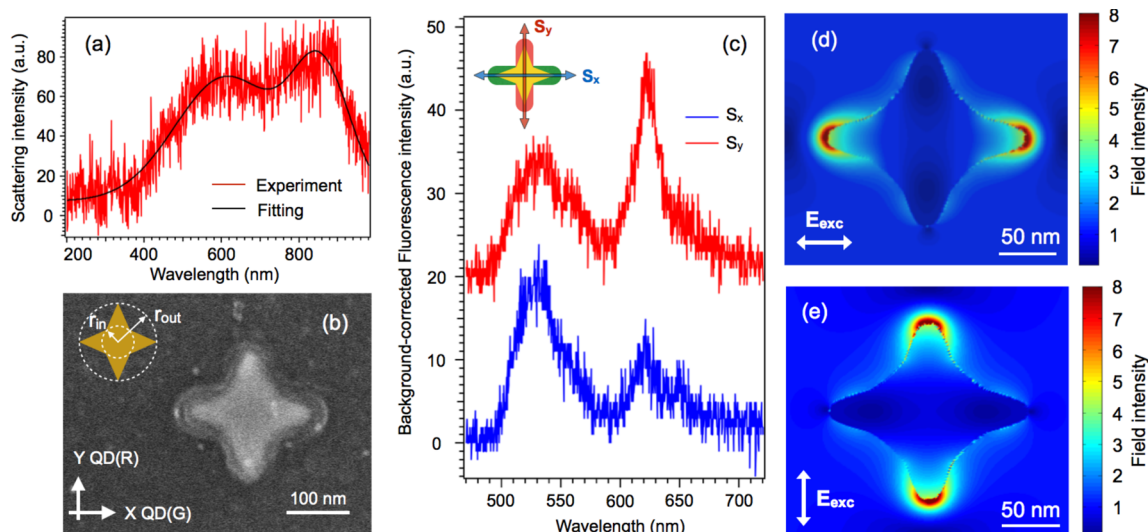


Figure 4. TCANE based on a gold nanostar. (a) Scattering spectrum of the initial gold nanostar before photopolymerization in air. (b) SEM image of a TCANE based on a nanostar (after two exposures). Red QDs are trapped along the Y axis and green QDs lie along the X axis. (c) Fluorescence spectra collected with the polarization of excitation light ($\lambda_{exc} = 405$ nm) along the X axis (blue) and Y axis (red). (d), (e) FDTD calculation of the field intensity in the vicinity of the nanostar on a glass substrate within polymer (refractive index = 1.5) for two incident polarization direction ($\lambda = 730$ nm). The mesh size was 1 nm.

We will come back later to this point in the section of [Interpretation and Theoretical Illustration](#).

The TCANE based on a gold nanodisk enables the selection of an emission mode of the nanoemitter. Both fluorescence intensity and the dominant wavelength can be controlled by the polarization of the incident light. It has to be stressed that the TPP can be applied generally on more complex shapes to achieve the TCANE behavior. We reproduced the fabrication of nanoemitters as well as the optical characterization based on a gold nanostar.

Nanostar-Based TCANE. Nanostars are attracting much attention because of the plasmonic lightning-rod effect at the end of each branch.^{47,48} Four-branch gold nanostars were fabricated using EBL on the ITO-coated glass substrate. The nanostar had an inner radius of $r_{in} = 50$ nm, an external radius of $r_{out} = 90$ nm (shown in the inset of Figure 4b), and a thickness of $h = 50$ nm. Figure 4a is the scattering spectrum of the nanostar in air. Peaks at 612 and 858 nm correspond to the inner and external diameters, respectively. Again, the green QDs were positioned along the X axis during the first exposure for photopolymerization, whereas the red QDs were trapped along the Y axis by the second exposure. Figure 4b shows the SEM image of the resulting TCANE based on the gold nanostar. Thanks to the lightning rod effect, polymer nanostructures are thicker at the ends of the branches as compared to the edges. Keeping in mind that the scattering spectrum shown in Figure 4a is red-shifted in polymer, it is assumed that the 730 nm wavelength mainly allowed for the excitation of an off-resonance lightning rod effect at the tips extremities, corresponding to electromagnetic singularities. We performed 3-D finite difference time domain (3-D FDTD) simulation of the intensity map in the vicinity of the nanostar during photo polymerization for both X and Y (see Figure 4d,e). For calculation, a realistic structure was used: it was numerically extracted from SEM images of the nanostar. The intensity enhancement factor of 8 is likely to be sufficient for local plasmonic photo polymerization at the tip extremities, resulting in hybrid nanostar shown in Figure 4b.

The nanostar-based TCANE was characterized optically by polarization-controlled fluorescence (Figure 4c). With an incident polarization parallel to the green QD-grafted nanoparticles (S_x), the emission of the green QDs is noticeably higher than that of the red QDs. When the polarization direction is flipped by 90° , the emission of red QDs is dominant. Again, the red emission mode is obviously more sensitive to the incident polarization than that of the green QDs, as already observed in Figure 3g.

Interpretation and Theoretical Illustration. The polarization sensitivity is interpreted on the basis of the spatial rotation of the near-field excitation rate Γ_{exc} , making it possible to selectively address “red” or “green” QDs. The rate of emission (the observable quantity Γ_{em}) is given by

$$\Gamma_{em} = Q\Gamma_{exc} \quad (1)$$

where Q is the apparent (or modified) quantum yield in the presence of the metal nanoparticle.

Q is defined as:

$$Q = \frac{\Gamma_{rad}}{\Gamma_{rad} + \Gamma_{nrad}} \quad (2)$$

where Γ_{rad} and Γ_{nrad} are the radiative decay rate and the nonradiative decay rate, respectively.

Γ_{exc} depends on the local field E_{loc} through the expression 3

$$\Gamma_{exc} \propto |p \cdot E_{loc}|^2 \quad (3)$$

where p is the transition dipole moment of the emitter. Recent studies have shown that spherical semiconducting quantum dots or dot-in-rods present a dipole moment of well-defined orientation in space.^{49,50} In our case, we consider that both orientation and spatial distribution of dipoles within the polymer are random (illustrated in Figure 5a and in the TEM image in the [Supporting Information](#)). The following calculations have been performed in the case of the TCANE geometry described in Figure 3. E_{loc} was calculated by the 3-D FDTD method. The spatial distribution of the modulus of E_{loc} at $\lambda = 405$ nm is shown in Figure 5b and c for Y and X incident

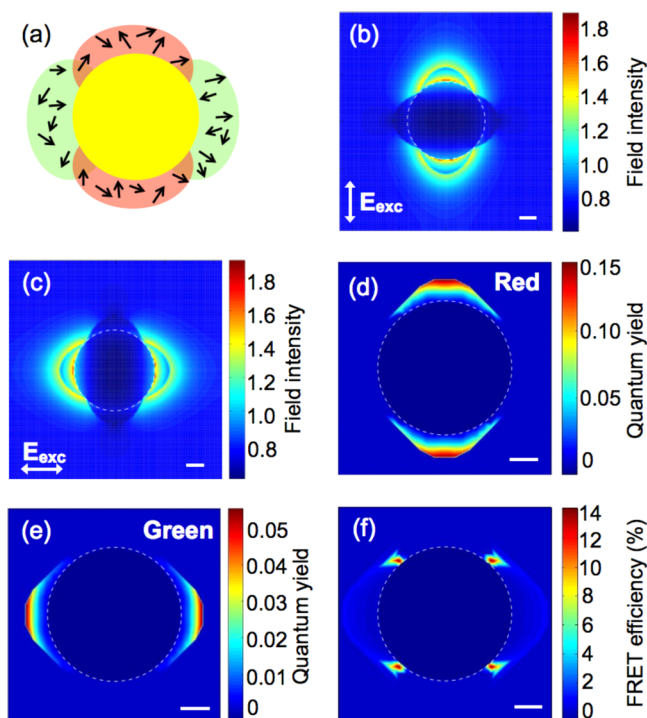


Figure 5. Simulation of the gold nanodisk-based TCANE. (a) Scheme of the TCANE with QD dipoles randomly oriented and located in the polymer nanostructures. (b) Field distribution with $\lambda_{\text{exc}} = 405$ nm excitation light polarized along the Y axis. (c) Field distribution with $\lambda_{\text{exc}} = 405$ nm excitation light polarized along X axis. (d) Quantum yield of the red QDs at emission wavelength $\lambda_{\text{em}} = 617$ nm. (e) Quantum yield of the green QDs at emission wavelength $\lambda_{\text{em}} = 521$ nm. (f) Efficiency of fluorescent resonant energy transfer from green QDs to red QDs. Scale bars represent 20 nm.

polarization, respectively. The calculation was performed with the realistic geometry of the hybrid structure (gold particle on the substrate, with four polymer lobes). Due to off-resonance excitation of gold, the field is pretty weak. At the resonance, it would be at least ten times stronger. However, even in a off-resonance situation, from Figure 5b,c, it turns out that the gold nanoparticle acts as an optical concentrator enabling both field confinement and polarization-controlled field rotation. More importantly, Figure 5b,c show that Γ_{exc} can be spatially confined. As a result, emitters can be selectively excited. Calculation of the different field components show that the orientation of the near-field is relatively well preserved with regard to the incident field direction, despite weak in-plane \rightarrow out-of-plane and X \leftrightarrow Y depolarization. For example, the value of the maximum modulus of the Y-polarized field component is 1.6 for Figure 5b (as compared to 1.8 for the total field intensity). As a result, considering eq 3, mainly Y-oriented dipoles are expected to be excited in Figure 5b. In the same way, mainly X-oriented dipoles are expected to be excited in Figure 5c.

The emitted signal is then estimated from eq 1. This expression can be polarization sensitive because Q is spatially anisotropic due to spatial distribution of the two types of QDs. Q was calculated for green and red emission wavelengths, taking again into account the realistic geometry, including the in-plane spatial distribution of two kinds of emitters. The principle of the calculation is described in the Methods section. The calculated modified quantum yield of red QDs and green

QDs are presented in Figure 5d and e, respectively. The apparent anisotropy in these maps results from the controlled anisotropy of color spatial distribution as shown in Figure 3. Both Figure 5d and e are characterized by a quenching zone in close proximity to the particle, whereas at 10 nm distance from the particle, the quantum yield is maximum. Y polarization results in an efficient spatial overlap between the quantum yield for red light (Figure 5d) and the local field (and thus the rate of excitation) shown in Figure 5b, whereas the good spatial overlap between Figure 5c and e is at the origin of dominant green emission for X polarization.

In Figure 3, we noted a difference in polarization sensitivities between the red and green QDs. With a Y polarization ($\theta = 0^\circ$), the emission of red QDs is modified by the plasmonic near-field, whereas the green QDs are excited mainly by the far-field. In comparison, the emission from green QDs is modified by the plasmonic near-field with a X incident polarization ($\theta = 90^\circ$). A subtracted fluorescence intensity of minimum spatial overlap from the complete overlap state, thus, will show the emission caused by a pure plasmonic field, that is, about 100 counts for the red QDs and about 40 counts for the green. The polarization sensitivity of the red QDs is, therefore, about 2.5 times that of the green QDs. When a similar near-field distribution for either X or Y polarization due to the symmetry of the nanodisks is considered, we can deduce that the key factor leading to the different polarization sensitivities of QDs is the quantum yield that is spatially selectively addressed. It reaches a maximum of 5.6% (Figure 5e) for the green QDs and 15% (Figure 5d) for the red QDs in Figure 5 (2.67 times that of the quantum yield of green QDs).

When considering the fluorescence intensity ratio of two extremes ($I_{\text{max}}/I_{\text{min}}$) of both types of QDs, one can deduce $I_{\text{max}}/I_{\text{min}} = 2$ for red QDs and $I_{\text{max}}/I_{\text{min}} = 1.56$ for green QDs. Quantum yield, as an intrinsic factor of QDs, is a constant that is independent from incident polarization angles. Because symmetric structure of nanodisk was used, the strength of the local optical electromagnetic field is not polarization dependent. This different $I_{\text{max}}/I_{\text{min}}$ obtained from two types of QDs can result from different absorption efficiency (refer to the absorption spectra in Supporting Information), where red QDs is 2 times higher than green QDs.

Finally, we stress that possible energy transfer between donors (green QDs) and acceptors (red QDs) can occur in the presence of the metal nanoparticle. This energy transfer has been calculated (see Methods) in the case of the four-lobe nanodisk-based TCANE. Figure 5f shows a map of (green \rightarrow red) energy transfer efficiency that is maximal where the two kinds of emitters are close to each other. This energy transfer from green to red QDs is likely to affect polarization sensitivity. In particular, this could be one of the reasons why red emission seems to be more sensitive to the polarization rotation than green emission is, as shown in Figure 3g. This effect opens new routes for plasmon-assisted short and long distance non-radiative energy transfer in hybrid plasmonics.⁵¹

To conclude, we reported plasmonic nanoemitters with two different emission wavelengths. The dominant wavelength can be selected by rotating the polarization of the incident light. The plasmonic nanoemitters were fabricated via surface plasmon-triggered two-photon nanophotopolymerization. By taking advantage of the dipolar distribution of the optical near-field, we successfully trapped green QDs along the X axis and red QDs along the Y axis through two-step photopolymerization. Distributed along different axes, different colors of QDs

can therefore be optically selected by the dipolar near-field of the excitation light, that is, incident polarization. The TCANEs fabrication technique is applicable not only to highly symmetric nanodisks but also to arbitrary shaped nanoparticles such as nanostars. For each TCANE, the dominant output color is sensitive to the incident state of polarization. Based on this point, the TCANEs have the potential to produce switchable plasmonic nanoemitters with considerable applications in nanophotonics. Numerous perspectives are envisioned. In particular, six-branch stars will be used for three-color TCANEs for new addressable RGB nanopixels and hot and cold spots in metal nanocubes⁵² will be exploited for more confined plasmonic fields that should enable better contrast and selection of output colors.

Methods. Grafting QDs on the PETIA Monomer. Green-emitting CdSe/ZnS QDs with chemical-composition gradients were prepared using a one-pot synthesis method,⁵³ and the red-emitting CdSe/CdS/ZnS core-shell structured QDs were prepared by the multiple injection method according to the same literature. For a typical preparation of green-emitting QDs, 0.1 mmol of cadmium oxide (CdO), 4 mmol of zinc acetate (Zn(Acet)₂), and 5 mL of oleic acid (OA) were loaded in a 50 mL 3-neck flask, heated to 150 °C under vacuum to form cadmium oleate (Cd(OA)₂) and zinc oleate (Zn(OA)₂). Then 20 mL of 1-octadecene (1-ODE) was added to the reaction flask and the reactor was then filled with nitrogen and heated up to 300 °C. At the elevated temperature, 1.6 mL of tri-*n*-octylphosphine (TOP) dissolving 0.15 mmol of selenium (Se) and 4 mmol of sulfur (S) was injected into the flask swiftly, and the reaction mixture was maintained at 300 °C for 10 min for the QD growth. For the synthesis of red-emitting QDs, 1 mmol of CdO, 2 mmol of Zn(Acet)₂, and 5 mL of OA were loaded in the 3-neck flask, heated to 150 °C under vacuum to form Cd(OA)₂ and Zn(OA)₂. Also, 25 mL of 1-ODE was added in the reaction flask and the reactor was then filled with nitrogen and heated up to 300 °C. At 300 °C, 0.2 mL of TOP dissolving 0.2 mmol of Se was injected into the flask swiftly. After 2.5 min, 0.3 mL of dodecanethiol (DDT) was slowly added into the reaction system and preceded at 300 °C for 20 min for the CdSe/CdZnS QD growth. Subsequently, 1 mL of TOP dissolving 2 mmol of S was then injected into the reaction flask to coat an additional ZnS shell on the CdSe/CdS/ZnS QDs and kept for 10 min. To purify the synthesized QDs, the reaction mixture was cooled down to room temperature, and the QDs were extracted by the addition of acetone and methanol, followed by centrifugation. The as-prepared QDs were finally dispersed in PETIA with a concentration of 5 mg/mL under vigorous magnetic stirring.

Two-Photon Polymerization: Threshold Determination and Configuration. The photopolymerization process was performed with a femtosecond laser at $\lambda = 730$ nm focused by a 100x/1.3NA water immersion objective. The photopolymerization step starts with determination of threshold, that is, lowest energy that fabricated a polymer dot on an ITO-coated glass substrate without the presence of metal nanoparticles. In this Letter, the threshold was measured as 0.3125 mJ·cm⁻² for both solutions. The dose of energy applied for fabricating the TCANEs was 0.1875 mJ·cm⁻².

Fluorescence Images and Spectra Collection. The fluorescence spectra and images were collected with a spectrometer that was coupled to an inverted microscope. A 60x/1.45NA oil immersion objective was adopted for signal collection. The light for fluorescence excitation was a $\lambda = 405$

nm continuous laser. To avoid any changes in the optical light path while switching the incident polarization, it was in fact the sample that was rotated on the microscope stage instead of the polarization of the incident light. The offset of the chosen particle in the nanoparticle array helped us to locate it precisely after the rotation of the sample. During alignment, the location of laser spot was first marked on the CCD live image. The nanoemitters were then aligned with the position of the mark (i.e., laser spot position). In this way, we put precisely the same nanoemitter at same position while rotating the sample. When collecting the fluorescence spectra, the sizes of spectrometer slits were variable, which made it possible to collect fluorescence signal from the single nanoemitter that has been aligned with the laser spot. The detecting area on the sample was about 1 $\mu\text{m} \times 1 \mu\text{m}$. Power at the microscope input was measured as 0.1 mW·cm⁻² and an acquisition time of 20 s was used for each spectra. In the case of a fluorescence image, the power measured at the microscope input was 0.8 mW·cm⁻². The acquisition time was 1 s.

Calculation of the Modified Quantum Yield. The quantum yield is defined by $Q = \Gamma_{\text{rad}}/\Gamma_{\text{tot}}$ where Γ_{rad} and Γ_{tot} are the radiative and total decay of the QDs in the presence of the MNP. Γ_{rad} and Γ_{tot} are calculated using the Green's dyad technique⁵⁴ by discretizing the metallic nanoparticle and where the variations of the Green's dyad S on each mesh is exactly included.⁵⁵ Γ_{rad} and Γ_{tot} strongly depends on the intrinsic quantum yield of the QD $q = \Gamma_0^{\text{rad}}/\Gamma_0$ without the metallic nanoparticle and express $\Gamma_{\text{rad}}/\Gamma_0 = 6\pi q/k_{\text{em}}\text{Im}[S(r_{\text{QD}}, r_{\text{QD}}, \omega_{\text{em}})]$ and $\Gamma_{\text{tot}}/\Gamma_0 = 1 + 6\pi q/k_{\text{em}}\text{Im}[S(r_{\text{QD}}, r_{\text{QD}}, \omega_{\text{em}})]$, respectively. The intrinsic quantum yield measured in the polymer matrix is $q = 64\%$ ($q = 69\%$) for red (green) QDs. r_{QD} refers to the position of the QD and to its ω_{em} emission wavelength. The energy transfer between green QDs at r_{green} and red QDs at r_{red} is proportional to $\text{Im}[S(r_{\text{green}}, r_{\text{red}}, \omega_{\text{green}})]$.^{56,57}

■ ASSOCIATED CONTENT

📄 Supporting Information

The Supporting Information is available free of charge on the ACS Publications website at DOI: 10.1021/acs.nanolett.5b02962.

Au nanoparticle size-dependent polymer thickness, absorption spectra of QD-doped PETIA solutions, original SEM images, TEM images on micron-size photopolymer, fluorescence reference spectra, and influence of ITO layer on the fluorescence intensity of QDs. (PDF).

Video showing the blinking of QDs (MOV).

■ AUTHOR INFORMATION

Corresponding Authors

*E-mail: (X.W.S.) exwsun@ntu.edu.sg.

*E-mail: (R.B.) renaud.bachelot@utt.fr.

Present Addresses

Department of Chemistry, University of Illinois at Urbana-Champaign, 600 S. Matthews Av. Urbana, IL 61801, United Kingdom. (X.Z.)

Department of Applied Physics, Ghent University, Technicum-Blok 2. Sint-Pietersnieuwstraat, 41 9000 Gent, Belgium. (J.W.)

Department of Physics and Mathematics, University of Hull, Cottingham Road, Hull, HU6 7RX, United Kingdom. (F.N.V.)

Notes

The authors declare no competing financial interest.

ACKNOWLEDGMENTS

The authors would like to thank the platform Nano'mat and the HAPPLE project (ANR-12-BS10-0016) funded by Agence Nationale de la Recherche (ANR). R.B. would like to thank the members of the HAPPLE consortium for fruitful discussion. This work was supported, in part (R.D.S. and G.P.W.), by the Center for Nanoscale Materials, a U.S. Department of Energy, Office of Science and Office of Basic Energy Sciences User Facility under Contract No. DE-AC02-06CH11357. X.W.S. would like to thank the support from the National Research Foundation of Singapore under its Competitive Research Program No. NRF-CRP11-2012-01 and No. NRF-CRP6-2010-2. The authors would like to give thanks to Dr. Prashant K. Jain for suggestions. The author would also like to acknowledge networking support by the COST Action IC1208, www.ic1208.com. This work has been done in the general context of the Labex ACTION program (ANR-11-LABX-01-01).

REFERENCES

- (1) Coldren, L. A.; Corzine, S. W.; Mashanovitch, M. L. *Diode Lasers and Photonic Integrated Circuits*; John Wiley & Sons: Hoboken, NJ, 2012.
- (2) Bergman, K.; Carloni, L. P.; Biberman, A.; Chan, J.; Hendry, G. *Photonic Network-on-Chip Design (Integrated Circuits and Systems)*; Springer: New York, 2014.
- (3) Hill, M. T.; Gather, M. C. *Nat. Photonics* **2014**, *8*, 908–918.
- (4) Akselrod, G. M.; Argyropoulos, C.; Hoang, T. B.; Ciraci, C.; Fang, C.; Huang, J.; Smith, D. R.; Mikkelsen, M. H. *Nat. Photonics* **2014**, *8*, 835–840.
- (5) Yang, A. Y.; Hoang, A. B.; Dridi, M.; Deeb, C.; Maiken, H.; Mikkelsen, M. H.; Schatz, J. C.; Odom, T. W. *Nat. Commun.* **2015**, *6*, 6939.
- (6) Stockman, M. I. *Nat. Photonics* **2008**, *2*, 327–329.
- (7) Cohen-Hoshen, E.; Bryant, G. W.; Pinkas, I.; Sperling, J.; Bar-Joseph, I. *Nano Lett.* **2012**, *12*, 4260–4264.
- (8) Zhang, Q.; Li, G.; Liu, X.; Qian, F.; Li, Y.; Sum, T. C.; Lieber, C. M.; Xiong, Q. *Nat. Commun.* **2014**, *5*, 4953.
- (9) Bardhan, R.; Grady, N. K.; Cole, J. R.; Joshi, A.; Halas, N. J. *ACS Nano* **2009**, *3*, 744–752.
- (10) Ming, T.; Zhao, L.; Yang, Z.; Chen, H.; Sun, L.; Wang, J.; Yan, C. *Nano Lett.* **2009**, *9*, 3896–3903.
- (11) Ringler, M.; Schwemer, A.; Wunderlich, M.; Nichtl, A.; Kurzinger, K.; Klar, A.; Feldmann, J. *Phys. Rev. Lett.* **2008**, *100*, 203002.
- (12) Shubina, T. V.; Toropov, A. A.; Jmerik, V. N.; Kuritsyn, D. I.; Gavrilenko, L. V.; Krasil'nik, Z. F.; Araki, T.; Nanishi, Y.; Gil, B.; Govorov, A. O.; Ivanov, S. V. *Phys. Rev. B: Condens. Matter Mater. Phys.* **2010**, *82*, 073304.
- (13) Khatua, S.; Paulo, P. M. R.; Yuan, H.; Gupta, A.; Zijlstra, P.; Orrit, M. *ACS Nano* **2014**, *8*, 4440–4449.
- (14) Guzatov, D. V.; Vaschenko, S. V.; Stankevich, V. V.; Lunevich, A. Y.; Glukhov, Y. F.; Gaponenko, S. V. *J. Phys. Chem. C* **2012**, *116*, 10723–10733.
- (15) Tam, F.; Goodrich, G. P.; Johnson, B. R.; Halas, N. J. *Nano Lett.* **2007**, *7*, 496–501.
- (16) Kinkhabwala, A.; Yu, Z.; Fan, S.; Avlasevich, Y.; Mullen, K.; Moerner, W. E. *Nat. Photonics* **2009**, *3*, 654–657.
- (17) Lu, G.; Li, W.; Zhang, T.; Yue, S.; Liu, J.; Hou, L.; Li, Z.; Gong, Q. *ACS Nano* **2012**, *6*, 1438–1448.
- (18) Langguth, L.; Puni, D.; Wenger, J.; Koenderink, A. F. *ACS Nano* **2013**, *7*, 8840–8848.
- (19) Curto, A. G.; Taminiau, T. H.; Volpe, G.; Kreuzer, M. P.; Quidant, R.; van Hulst, N. F. *Nat. Commun.* **2013**, *4*, 1750.
- (20) Hartling, T.; Reichenbach, P.; Eng, L. M. *Opt. Express* **2007**, *15*, 12806–12817.
- (21) Dulkeith, E.; Morteaux, A. C.; Niedereichholz, T.; Klar, T. A.; Feldmann, J. *Phys. Rev. Lett.* **2002**, *89*, 203002.
- (22) Anger, P.; Bharadwaj, P.; Novotny, L. *Phys. Rev. Lett.* **2006**, *96*, 113002.
- (23) Kuhn, S.; Hakanson, U.; Rogobete, L.; Sandoghdar, V. *Phys. Rev. Lett.* **2006**, *97*, 017402.
- (24) Noginov, M. A.; Zhu, G.; Belgrave, A. M.; Bakker, R.; Shalae, V. M.; Narimanov, E. E.; Stout, S.; Herz, E.; Suteewong, T.; Wiesner, U. *Nature* **2009**, *460*, 1110–1113.
- (25) Ming, T.; Zhao, L.; Chen, H.; Woo, K. C.; Wang, J.; Lin, H.-Q. *Nano Lett.* **2011**, *11*, 2296–2303.
- (26) Curto, A. G.; Volpe, G.; Taminiau, T. H.; Kreuzer, M. P.; Quidant, R.; van Hulst, N. F. *Science* **2010**, *329*, 930–933.
- (27) Muskens, O. L.; Giannini, V.; Sanchez-Gil, G. A.; Gomez Rivas, J. *Nano Lett.* **2007**, *7*, 2871–2875.
- (28) Zhou, X.; Deeb, C.; Kostcheev, S.; Wiederrecht, G. P.; Adam, P.-M.; Béal, J.; Plain, J.; Gosztola, D. J.; Grand, J.; Féridj, N.; Wang, H.; Vial, A.; Bachelot, R. *ACS Photonics* **2015**, *2*, 121–179.
- (29) Andreozzi, P.; Martinelli, C.; Carney, R. P.; Carney, T. M.; Stellacci, F. *Mol. Pharmaceutics* **2013**, *10*, 875–882.
- (30) Guero, Z.; Libchaber, A. *Phys. Rev. Lett.* **2004**, *93*, 166108.
- (31) Kelly, K. L.; Coronado, E.; Zhao, L. L.; Schatz, G. C. *J. Phys. Chem. B* **2003**, *107*, 668–677.
- (32) Jain, P. L.; El-Sayed, M. A. *Chem. Phys. Lett.* **2003**, *487*, 153–164.
- (33) Wang, H.; Brandl, D. W.; Le, F.; Nordlander, P.; Halas, N. *Nano Lett.* **2006**, *6*, 827–832.
- (34) Huang, X.; Neretina, S.; El-Sayed, M. A. *Adv. Mater.* **2009**, *21*, 4880–4910.
- (35) Rechberger, W.; Hohenau, A.; Leitner, A.; Krenn, J. R.; Lamprecht, B.; Aussenegg, F. R. *Opt. Commun.* **2003**, *220*, 137–141.
- (36) Wei, H.; Reyes-Coronado, A.; Nordlander, P.; Aizpurua, J.; Xu, Y. *ACS Nano* **2010**, *4*, 2649–2654.
- (37) Wurtz, G. A.; Dickson, W.; O'Connor, D.; Atkinson, R.; Hendren, W.; Evans, P.; Pollard, R.; Zayats, A. V. *Opt. Express* **2008**, *16*, 7460–7470.
- (38) Zhao, L.; Ming, T.; Shao, L.; Chen, H.; Wang, J. *J. Phys. Chem. C* **2012**, *116*, 8287–8296.
- (39) Meng, X.; Kildishev, A. V.; Fujita, K.; Tanaka, K.; Shalae, V. M. *Nano Lett.* **2013**, *13*, 4106–4112.
- (40) Wu, X.; Reed, H. A.; Rhodes, L. F.; Elce, E.; Ravikiran, R.; Shick, R. A.; Henderson, C. L.; Allen, S. A. B.; Kohl, P. A. *J. Appl. Polym. Sci.* **2003**, *88*, 1186–1195.
- (41) Deeb, C.; Ecoffet, C.; Bachelot, R.; Plain, J.; Bouhelier, A.; Soppera, O. *J. Am. Chem. Soc.* **2011**, *133*, 10535–10542.
- (42) Deeb, C.; Bachelot, R.; Plain, J.; Baudrion, A.-L.; Jradi, S.; Bouhelier, A.; Soppera, O.; Jain, P. K.; Huang, L.; Ecoffet, C.; Balan, L.; Royer, P. *ACS Nano* **2010**, *4*, 4579–4586.
- (43) Deeb, C.; Zhou, X.; Miller, R.; Gray, S. K.; Marguet, S.; Plain, J.; Wiederrecht, G. P.; Bachelot, R. *J. Phys. Chem. C* **2012**, *116*, 24734–24740.
- (44) Ibn El Ahrach, H.; Bachelot, R.; Vial, A.; Lerondel, G.; Plain, J.; Royer, P.; Soppera, O. *Phys. Rev. Lett.* **2007**, *98*, 107402.
- (45) Gruber, C.; Hirzer, A.; Schmidt, V.; Trügler, A.; Hohenester, U.; Ditlbacher, H.; Hohenau, A.; Krenn, J. R. *Appl. Phys. Lett.* **2015**, *106*, 081101.
- (46) Ueno, K.; Juodkazis, S.; Shibuya, T.; Yokota, Y.; Mizeikis, V.; Sasak, K.; Misawa, H. *J. Am. Chem. Soc.* **2008**, *130*, 6928–6929.
- (47) Hrelescu, C.; Sau, T. K.; Rogach, A. L.; Jackel, F.; Laurent, G.; Douillard, L.; Charra, F. *Nano Lett.* **2011**, *11*, 402–407.
- (48) Dondapati, S. K.; Sau, T. K.; Hrelescu, C.; Klar, T. A.; Stefani, F. D.; Feldmann, J. *ACS Nano* **2010**, *4*, 6318–6322.
- (49) Lethiec, C.; Pisanello, F.; Carbone, L.; Bramati, A.; Coolen, L.; Maitre, A. *New J. Phys.* **2014**, *16*, 093014.
- (50) Lethiec, C.; Laverdant, J.; Vallon, H.; Javaux, C.; Dubertret, B.; Frigerio, J.-M.; Schwob, C.; Coolen, L.; Maitre, A. *Phys. Rev. X* **2014**, *4*, 021037.
- (51) Xu, H.; Liu, J.; Duan, X.; Li, J.; Xue, J.; Sun, X.; Cai, Y.; Zhou, Z.-K.; Wang, X. *Opt. Mater. Express* **2014**, *4*, 2586–2594.

(52) Haggui, M.; Dridi, M.; Plain, J.; Marguet, S.; Perez, H.; Schatz, G. C.; Wiederrecht, G. P.; Gray, S. K.; Bachelot, R. *ACS Nano* **2012**, *6*, 1299–1307.

(53) Bae, W. K.; Kwak, J.; Lim, J.; Lee, D.; Nam, M. K.; Char, K.; Lee, C.; Lee, S. *Nano Lett.* **2010**, *10*, 2368–2373.

(54) Colas des Francs, G.; Girard, C.; Bruyant, A.; Dereux, A. *J. Microsc.* **2008**, *229*, 302–306.

(55) Ould Agha, Y.; Demichel, O.; Girard, C.; Bouhelier, A.; Colas des Francs, G. *Prog. Electromagn. Res.* **2014**, *146*, 77–88.

(56) Colas des Francs, G.; Girard, C.; Martin, O. *Phys. Rev. A: At, Mol., Opt. Phys.* **2003**, *67*, 53805.

(57) Alejandro Gonzaga-Galeana, J.; Zurita-Sanchez, J. R. *J. Chem. Phys.* **2013**, *139*, 244302.